

Cite this: *Nanoscale Adv.*, 2020, 2, 5352

# Optimisation of the thermoelectric efficiency of zirconium trisulphide monolayers through uniaxial and biaxial strain†

Fernan Saiz, \*<sup>a</sup> Jesús Carrete <sup>b</sup> and Riccardo Rurali <sup>c</sup>

The goal of this work is to investigate the influence of mechanical deformation on the electronic and thermoelectric properties of ZrS<sub>3</sub> monolayers. We employ density functional theory (DFT) calculations at the hybrid HSE06 level to evaluate the response of the electronic band gap and mobilities, as well as the thermopower, the electrical conductivity, the phononic and electronic contributions to the thermal conductivity, and the heat capacity. Direct examination of the electronic band structures reveals that the band gap can be increased by up to 17% under uniaxial strain, reaching a maximum value of 2.32 eV. We also detect large variations in the electrical conductivity, which is multiplied by 3.40 under a 4% compression, but much smaller changes in the Seebeck coefficient. The effects of mechanical deformation on thermal transport are even more significant, with a nearly five-fold reduction of the lattice thermal conductivity under a biaxial strain of -4%. By harnessing a combination of these effects, the thermoelectric figure of merit of strained ZrS<sub>3</sub> could be doubled with respect to the unstrained material.

Received 24th June 2020  
Accepted 13th October 2020

DOI: 10.1039/d0na00518e

rsc.li/nanoscale-advances

## 1 Introduction

Strain engineering is an emerging field that tries to optimize the performance of materials,<sup>1,2</sup> and in particular, of 2D compounds such as graphene,<sup>3,4</sup> arsenene and phosphorene,<sup>5</sup> molybdenum disulphide<sup>6</sup> or titanium disulphide<sup>7,8</sup> for particular applications through the use of mechanical deformations. Strain engineering can be also applied to transition metal trichalcogenides<sup>9,10</sup> (MX<sub>3</sub> with M = Ti, Zr, or Hf and X = S, Se, or Te), which have recently attracted significant attention due to their narrow band gaps between 1.0 and 2.0 eV (ref. 11) that render their nanosheets suitable not only for optical and electronic applications,<sup>12</sup> but also as building blocks in thermoelectric devices.<sup>1,13</sup> For thermoelectric applications, the ongoing efforts to increase their efficiency must target their dimensionless figure of merit,  $zT$ , defined as

$$zT = \frac{S^2\sigma}{\kappa_{\text{el}} + \kappa_{\text{ph}}} T, \quad (1)$$

where  $S$  is the thermopower or Seebeck coefficient,  $\sigma$  is the electrical conductivity, and  $\kappa_{\text{el}}$  and  $\kappa_{\text{ph}}$  are the electronic and

phononic contributions to the thermal conductivity, respectively. Thus, new monolayer trichalcogenide nanosheets produced by chemical vapour deposition or multilayers obtained by mechanical exfoliation are designed to exhibit higher Seebeck coefficients and electrical conductivities and lower the thermal conductivities. Once these two-dimensional nanostructures are built, their power factor  $\sigma S^2$  can be further optimised through applied strain, given that their electronic structures near the Fermi level are influenced by the stretching or shrinking of the molecular bonds.<sup>14,15</sup> At the same time, displacing atoms from their original equilibrium positions alters their interactions, and hence the phonon dispersions<sup>16</sup> and the anharmonic force constants, which can lead to significant changes in the lattice thermal conductivity.

Another feature to be considered with a view to maximising the thermoelectric efficiency of layered trichalcogenides is the anisotropy of their thermal and electronic properties. For instance, in a recent work<sup>17</sup> we have shown that the thermal conductivity of TiS<sub>3</sub> monolayers and bilayers is highly dependent on the in-plane direction, with values at 300 K of 8.85 W m<sup>-1</sup> K<sup>-1</sup> in the  $x$ -direction and 13.56 W m<sup>-1</sup> K<sup>-1</sup> along the  $y$ -axis (the reference system is the same used here for ZrS<sub>3</sub> and illustrated in Fig. 1). Moreover, under a 7% compression the electrical conductivity of TiS<sub>3</sub> monolayers, and therefore their power factor, can nearly double in value with respect to the undeformed case.<sup>18</sup> Apart from TiS<sub>3</sub>, little is known about the thermoelectric potential of other trichalcogenides. A recent study has compared the thermoelectric performances of the bulk phase and a monolayer of zirconium trisulphide (ZrS<sub>3</sub>),<sup>19</sup> showing that the thermoelectric properties of the latter are

<sup>a</sup>Institut de Ciència de Materials de Barcelona (ICMAB-CSIC), Campus de la UAB, Bellaterra, 08193, Spain. E-mail: fsaiz@icmab.es

<sup>b</sup>Institute of Materials Chemistry, TU Wien, Getreidemarkt 9, 1060 Vienna, Austria. E-mail: jesus.carrete.montana@tuwien.ac.at

<sup>c</sup>Institut de Ciència de Materials de Barcelona (ICMAB-CSIC), Campus de la UAB, Bellaterra, 08193, Spain. E-mail: rrurali@icmab.es

† Electronic supplementary information (ESI) available. See DOI: 10.1039/d0na00518e



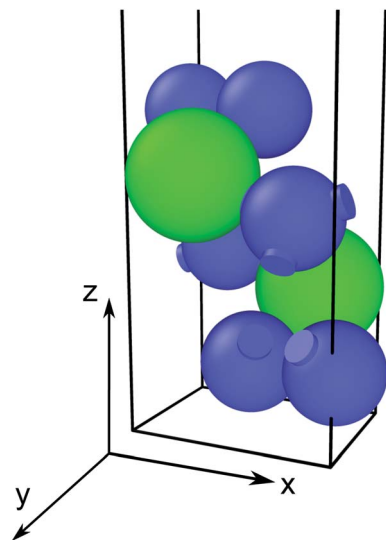


Fig. 1 Ball-and-stick representation of the  $\text{ZrS}_3$  monolayer, with sulphur atoms depicted in blue and zirconium atoms in green.

anisotropic, a feature also exhibited by  $\text{TiS}_3$  in a number of experimental and theoretical studies.<sup>17,20,21</sup> However, it is not clear if and how the interplay of anisotropy and strain can be harnessed to optimise the conversion of heat into electricity in  $\text{ZrS}_3$  monolayers.

The goal of this work is thus to evaluate how the thermoelectric properties of zirconium trisulphide monolayers behave under strain. We use total energy first-principles calculations to obtain electronic and thermal properties such as electronic mobilities and band gaps, Seebeck coefficients, and electrical and thermal conductivities for a number of strains applied either uniaxially or biaxially to  $\text{ZrS}_3$  nanosheets. Those nanosheets are represented as a vacuum gap in contact with a unit cell whose atomic structure is optimised within density functional theory (DFT). We employ plane waves to represent the electronic wave functions, and the generalised gradient approximation (GGA) to the exchange and correlation energies as a starting point. We then recalculate the electronic structure using the hybrid exchange-correlation functional HSE06,<sup>22</sup> which corrects the underestimated electronic band gap of the GGA calculation and substantially improves the agreement with the experimental values reported for  $\text{ZrS}_3$  nanostructures. Moreover, we compute the thermal properties of  $\text{ZrS}_3$  monolayers with a similarly fully *ab initio* approach starting from the relaxed atomic structure, paying attention to dynamical stability.  $\text{ZrS}_3$  is an n-type<sup>23</sup> semiconductor with a direct optical band gap of  $(2.02 \pm 0.02)$  eV, as measured in multilayered samples with an average thickness of  $(37 \pm 2)$  nm.<sup>24</sup> Previous measurements,<sup>23</sup> performed on single-crystal nanostructures 10 mm in length, 1 mm in width, and a few microns in thickness, showed that this material has an outstanding thermopower of  $-850 \mu\text{V K}^{-1}$  measured at 300 K, with an electrical conductivity of  $15 (\Omega \text{ cm})^{-1}$  and an electron mobility of  $25.98 \text{ cm}^2 \text{ V}^{-1} \text{ s}^{-1}$  for a charge carrier concentration of  $4.5 \times 10^{18}$  electrons per  $\text{cm}^3$ . Those measurements correspond to

transport along the atomic chains, *i.e.*, the direction represented as the  $y$  axis in Fig. 1. A few years later, the electrical properties of  $\text{ZrS}_3$  crystals on a  $\text{WSe}_2$  substrate at 289 K were reported as  $\sigma = 0.038 (\Omega \text{ cm})^{-1}$  and  $\mu = 10.3 \text{ cm}^2 \text{ V}^{-1} \text{ s}^{-1}$  at a concentration of  $2.33 \times 10^{16} \text{ e}^-$  per  $\text{cm}^3$ ,<sup>25</sup> along with a maximum Hall mobility of  $29.1 \text{ cm}^2 \text{ V}^{-1} \text{ s}^{-1}$  at 144 K. More recently, suspended plates of  $\text{ZrS}_3$  yielded an electron mobility of  $1132.9 \text{ cm}^2 \text{ V}^{-1} \text{ s}^{-1}$  and an electrical conductivity of  $0.12 (\Omega \text{ cm})^{-1}$  at a concentration of  $0.66 \times 10^{15}$  electrons per  $\text{cm}^3$ .<sup>26</sup> In this case, the suspended samples were fixed with silver paste on four contacts, which highlights to the key role of the substrate employed in the mobility measurements. We use those values as a reference to validate our calculations.

After this introduction, this manuscript is organised as follows. In Sec. 2, we detail the methodology employed to compute the charge mobilities, effective masses, Seebeck coefficients and other relevant thermoelectric quantities of  $\text{ZrS}_3$  monolayers under uniaxial and biaxial deformation. Next, in Sec. 3 we study the influence of stretching and compression on the electronic and thermal transport properties of the monolayer and evaluate the resulting figure of merit in order to detect the best strategies to increase the thermoelectric efficiency of those nanostructures. Finally, Sec. 4 presents our main findings and their implications for future work.

## 2 Theoretical methods

We use the Vienna *Ab initio* Simulation Package<sup>27–30</sup> (VASP) to relax the positions and cell parameters of the  $\text{ZrS}_3$  monolayer models. Those are initially represented as a unit cell belonging to the  $P2_1/m$  space group, as shown in Fig. 1. Reciprocal space integrations are performed using a mesh of  $10 \times 14 \times 1$   $k$  points centred at the  $\Gamma$  point. The geometry relaxation is carried out with thresholds of  $1 \times 10^{-8} \text{ eV nm}^{-1}$  for the forces and  $1 \times 10^{-8} \text{ eV}$  for the self-consistent solution of the electronic problem. These rather stringent thresholds are chosen so as to clearly identify those deformations that lead to imaginary phonon frequencies, *i.e.*, to mechanical instability. We use the generalised gradient approximation to the exchange and correlation potential in the form proposed by Perdew, Burke, and Ernzerhof<sup>31</sup> (PBE) and the projector-augmented wave method (PAW) to account for the core electrons.<sup>32,33</sup> The valence orbitals are expanded on a plane-wave basis with an energy cutoff of 350 eV. This value is chosen after a convergence test of the total energy with respect to this parameter. Long-range van der Waals forces are included using Grimme's zero-damping DFT-D3 scheme.<sup>34</sup> We include a vacuum layer of 1.4 nm to minimize the artifacts introduced by the periodic boundary conditions.

Once the geometry of the  $\text{ZrS}_3$  monolayer is relaxed, we obtain the following values for the moduli of the lattice vectors:  $a = 0.512 \text{ nm}$  and  $b = 0.363 \text{ nm}$ . We then apply uniaxial and biaxial strains from  $-4.0\%$  to  $7.0\%$  along the  $x$  and/or  $y$  directions in increases of  $1\%$ , keeping the lattice vector along the  $z$  axis, *i.e.* the vacuum layer thickness, constant. In this range of strains we always find exclusively real phonon frequencies, which points to the dynamical stability of the strained systems



investigated. For uniaxial strains exerted along the  $x$  (or  $y$ ) direction, the cell is allowed to adjust along the  $y$  (or  $x$ ) axis, thus enabling a straightforward calculation of the in-plane components of the Poisson's ratio. We then employ the HSE06 functional<sup>22</sup> to obtain the electronic structure of the optimised structures, from which we can obtain more reliable thermoelectric transport properties using the BoltzTraP code.<sup>35</sup> This code uses semiclassical Boltzmann theory under the uniform single-mode relaxation time approximation, and therefore the results for the electrical conductivity and the electronic contribution to the thermal conductivity are proportional to that parameter. The carriers' relaxation time is defined as

$$\tau_i = \frac{\mu_i m_i^*}{e}, \quad (2)$$

using Bardeen and Shockley's deformation potential theory.<sup>36</sup> The mobility along the  $i$ -th direction ( $\mu_i$ ) is estimated using the expression

$$\mu_i = \frac{2}{3} \frac{\hbar^3 C_{ii}}{k_B T (m_i^*)^2 E_{1,i}^2} \quad (3)$$

for a uniaxial or biaxial strain  $\varepsilon_i$ , where  $E_{1,i}$  is the deformation constant of Bardeen and Shockley's theory and  $C_{ii}$  is the relevant elastic constant for each deformation.  $E_{1,i}$  is calculated as the variation of the valence band maximum for holes and conduction band minimum for electrons with respect to the vacuum level vs. the strain. The elastic constants are obtained using the expression

$$C_{ii} = \frac{1}{A_0} \frac{\partial^2 E_{\text{tot}}}{\partial \varepsilon_i^2}, \quad (4)$$

where  $E_{\text{tot}}$  is the total energy per unit cell from the simulation and  $A_0$  is the area per unit cell of the unstrained monolayer. The elastic and deformation constants are determined from a series of PBE simulations where the monolayer is placed under strains from  $-2.0\%$  to  $2.0\%$  in increases of  $0.5\%$  along the two in-plane directions. The effective mass is determined from the dispersion relation for the  $l$ -th band using the parabolic approximation

$$E_l(k_i) = E_{0,l}(k_i) + \left( \frac{\hbar^2}{2m_{ij,l}^*} \right) (k_i - k_{i,0})^2, \quad (5)$$

where  $E_{0,l}(k_i)$  is the energy band maximum or minimum,  $m_{ij,l}^*$  is the effective mass for holes if we fit for the valence band maximum and electrons for the conduction band minimum, and  $k_{i,0}$  is the wave vector at the position of those extrema. We carefully checked that the band gap is direct for all strains between  $-4.0\%$  and  $7.0\%$ ; thus, the fit is performed around the  $\Gamma$  point along the  $x$  and  $y$  directions in reciprocal space.

We now describe the workflow employed to calculate the thermal transport properties of ZrS<sub>3</sub> monolayers. We use the almaBTE<sup>37</sup> package, which needs matrices of second- and third-order interatomic force constants (IFCs) from supercells. These force constants are obtained with VASP using the same computational parameters described above with the exception of the reciprocal-space integration grid, which now consists only of the  $\Gamma$  point for each one of the displaced supercell

configurations. Those configurations are generated by replicating the unit cell  $4 \times 5$  times with Phonopy<sup>38</sup> and thirdorder.py.<sup>39</sup> A cutoff of  $0.44$  nm (*i.e.*, up to the seventh nearest neighbors) is chosen for the third-order calculation. Due to the periodic boundary conditions and the corresponding breakdown of continuous rotation symmetry, the phonon frequencies of 2D systems calculated using this method are known to include numerical errors that can lead to the appearance of artificial imaginary acoustic frequencies near  $\Gamma$ .<sup>18,40,41</sup> Therefore, we need to apply a correction<sup>42</sup> to enforce the rotational symmetry in our calculations. After this correction is applied, analysis of the phonon dispersion curves for all strains applied reveals that the structure becomes unstable for uniaxial and biaxial compressive strains higher than  $4\%$ , with non-negligible negative acoustic frequencies near  $\Gamma$ .

We also computed the Born effective charges in order to include the non-analytic corrections that, in 3D systems, result in a splitting of the transverse and longitudinal optical phonon branches at the  $\Gamma$  point. However, recent theoretical and experimental studies have shown that such a splitting is suppressed in 2D materials because of the fundamentally different physics of polar 2D vs. 3D systems regarding the effect of the dipole-dipole interactions.<sup>43,44</sup>

Once all force constants are computed, we use them as inputs to solve the Boltzmann Transport Equation (BTE) self-consistently<sup>45</sup> and obtain the lattice thermal conductivity as

$$\kappa_{ij} = \sum_{\lambda} \kappa_{ij,\lambda} = K_1 \sum_{\lambda} f_{\lambda} (f_{\lambda} + 1) (\hbar v_{\lambda})^2 v_{i,\lambda} F_{j,\lambda}, \quad (6)$$

where  $i$  and  $j$  are Cartesian directions ( $x$  or  $y$ ),  $K_1^{-1} = k_B T^2 \Omega N$ ,  $k_B$  is Boltzmann's constant,  $\hbar$  is the Planck constant,  $\Omega$  the unit cell volume (excluding the vacuum layer), and  $N$  the number of  $q$  points used to sample the Brillouin zone. The summation in eqn (6) runs over all sampled phonon modes  $\lambda$ ; each mode has a frequency  $\nu_{\lambda}$  and a group velocity  $v_{\lambda}$ , and at thermal equilibrium at temperature  $T$  its occupancy follows the Bose-Einstein distribution  $f_{\lambda}$ .  $F_{j,\lambda}$  is first initialized to  $\tau_{\lambda} v_{j,\lambda}$ , where  $\tau_{\lambda}$  is the lifetime of mode  $\lambda$  within the relaxation time approximation (RTA). Starting from this guess, the solution is then obtained recursively and  $F_{j,\lambda}$  takes the general form  $\tau_{\lambda} (v_{j,\lambda} + \Delta_{j,\lambda})$ , where the correction  $\Delta_{\lambda}$  captures the changes in the occupancies associated to deviations from the RTA.<sup>46,47</sup> Phonon scattering due to isotopic disorder is also included under the Tamura approximation,<sup>48</sup> considering the natural distributions of Zr and S isotopes.

## 3 Results and discussion

### 3.1 Electron mobilities

Tables 1 and 2 summarize the values of the elastic constants  $C$  of the monolayers, the deformation potential constants  $E_1$ , the effective masses  $m^*$ , the mobilities  $\mu$ , and the relaxation times  $\tau$  of holes and electrons in the  $x$  and  $y$  directions, calculated for undeformed monolayers using HSE06. Our electron mobilities overestimate the experimental values,<sup>23,25,26</sup> a phenomenon also reported in other trichalcogenides such in TiS<sub>3</sub>.<sup>17,20,21</sup> This discrepancy can, *a priori*, be attributed to different sets of



**Table 1** Elastic constants  $C$  (eV  $\text{\AA}^{-2}$ ), deformation potential constants  $E_1$  (eV), effective masses  $m^*$  (in units of the electron mass  $m_0^*$ ), mobilities  $\mu$  ( $\text{cm}^2 \text{V}^{-1} \text{s}^{-1}$ ), and relaxation times  $\tau$  (fs) of holes and electrons obtained after applying strains in the  $x$  ( $\epsilon_x$ ) and  $y$  ( $\epsilon_y$ ) directions, calculated using the HSE06 functional, for undeformed monolayers

Strain	Carrier	$C$	$E_1$	$m^*$	$\mu$	$\tau$
$\epsilon_x$	Hole	5.48	-1.03	-0.54	4038.27	1235.28
$\epsilon_y$	Hole	8.09	-7.16	-0.97	37.90	20.97
$\epsilon_x$	Electron	5.48	0.39	1.65	3004.82	2826.12
$\epsilon_y$	Electron	8.09	3.43	0.29	1810.53	302.45

**Table 2** Elastic constants  $C$  (eV  $\text{\AA}^{-2}$ ), deformation potential constants  $E_1$  (eV), effective masses  $m^*$  (in units of the electron mass  $m_0^*$ ), mobilities  $\mu$  ( $\text{cm}^2 \text{V}^{-1} \text{s}^{-1}$ ), and relaxation times  $\tau$  (fs) of holes and electrons obtained after applying biaxial ( $\epsilon_b$ ) deformations, calculated using the HSE06 functional, for undeformed monolayers

Strain	Carrier	$C$	$E_1$	$m^*$	$\mu$	$\tau$
$\epsilon_b$	Hole	15.81	-8.04	-0.54	192.31	58.83
$\epsilon_b$	Hole	15.81	4.36	-0.97	199.18	110.24
$\epsilon_b$	Electron	15.81	-8.04	1.65	20.34	19.13
$\epsilon_b$	Electron	15.81	4.36	0.29	2186.61	365.27

factors, like an inaccurate determination of the mobility or the different conditions at which measurements and simulations are made.

Regarding the calculation of mobility from DFT using eqn (3), the disagreement may be caused by an incorrect calculation of the effective mass  $m^*$  or of the constant  $E_1$  from deformation potential theory (or both) or by limitations of the formalism itself *versus* a more detailed treatment of electron-phonon scattering. However, it seems reasonable to assume that the HSE06 functional likely reproduces the shape of the conduction band in reciprocal space fairly well for two reasons. First, we

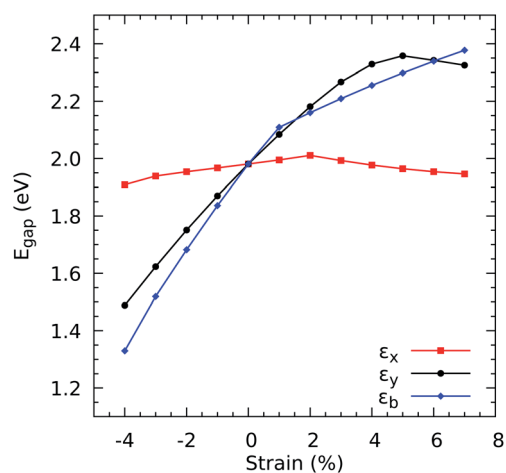


**Fig. 2** Electronic band gaps  $E_{\text{gap}}$ , calculated using the HSE06 functional, as a function of the uniaxial strains, ( $\epsilon_x$ ) and ( $\epsilon_y$ ), and the biaxial strain, ( $\epsilon_b$ ).

find a very good agreement of the experimental optical and electronic band gaps; second, our hole effective masses are in excellent agreement with the values of  $-0.87 (\pm 0.09) m_e$  along the  $x$  axis and  $-0.49 (\pm 0.20) m_e$  along the  $y$  axis recently measured on  $\text{ZrS}_3$  nano-whiskers using nanospot angle resolved photoemission spectroscopy (nanoARPES).<sup>49</sup>

If we analyse the conditions at which simulations and experiments are carried out, we find the following factors that can be responsible for the disagreement: first, the  $\text{ZrS}_3$  samples in the experiments are multilayers rather than the monolayer we model with DFT; second, these samples can contain crystallographic defects or surface impurities as well as slightly different compositions that deviate from their ideal stoichiometry; and third, the samples were measured with different substrates. The first cause can be expected to have only a minor impact because the band gap of the experimental multilayer<sup>24</sup> is very similar to that reported in the bulk<sup>19</sup> and computed for the monolayer in this work. The second factor is likely to play a more significant role since the presence of crystallographic defects cannot be completely ruled out. Moreover, the stoichiometry of exfoliated  $\text{ZrS}_3$  layers has been reported to differ from the ideal ratio  $\text{S}/\text{Zr} = 3/1$ , which might *a priori* produce relevant changes in the electronic structure. Additionally, a strong influence is also exerted by the substrate employed to encapsulate the sample in the laboratory setup. For instance, the data provided in ref. 23 and 25 differs from that published in ref. 26. The first study used samples suspended on four gold contacts, while the second work employed  $\text{WSe}_2$  as a substrate, and the

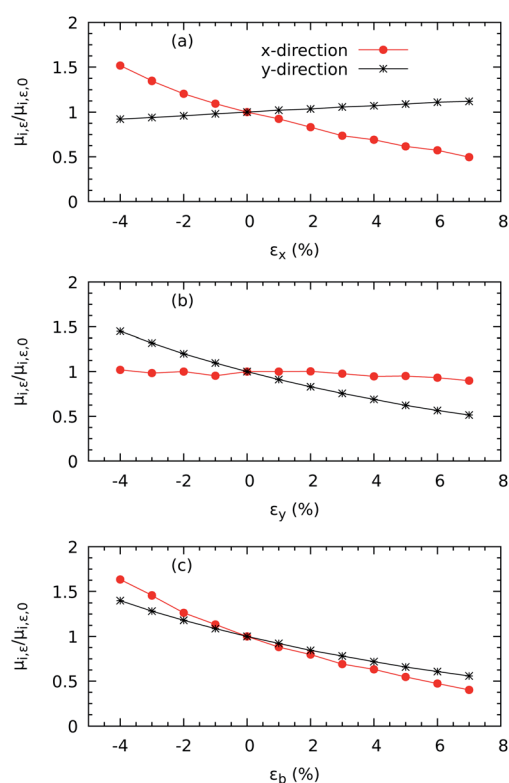


**Fig. 3** Electronic mobilities vs. uniaxial strains using the HSE06 functional along the  $x$  (a) and  $y$  (b) directions and biaxial strains (c).



third fixed the samples with four silver contacts. Since silver is the best conductor among the three materials, it is to be expected that the highest mobility be recorded with this material.

### 3.2 Band gaps

For the purposes of work, we determine the electronic band gap as the difference between the conduction band minimum and valence band maximum for the PBE and HSE06 functionals. This formulation yields band gaps of 1.09 eV for PBE and 1.99 eV for HSE06. Since HSE06 is able to provide an excellent agreement with the experimental optical band gap, we stick to HSE06 when calculating the properties necessary to obtain the figure of merit for ZrS<sub>3</sub> under strain. Fig. 2 shows that the HSE06 band gap responds anisotropically to mechanical stress: on the one hand, it only decreases slightly when compression and stretching are applied in the *x* direction (*i.e.*, perpendicular to the chains), with changes smaller than 4% for  $\varepsilon_x = -4\%$ ; on the other hand, it gets narrowed by  $-24.9\%$ , down to 1.49 eV, under a strain  $\varepsilon_y = -4\%$ , and grows with increasingly positive  $\varepsilon_y$  up to 2.33 eV, which represents a widening by 17.30%. The behavior under biaxial deformation is similar to the response to  $\varepsilon_y$  alone, suggesting that the latter drives the former.

Another crucial electronic property in n-type semiconductors, such as ZrS<sub>3</sub>, is the electron mobility, which dictates how fast an electron can move through the lattice, in effective terms, under the effect of an electric field. In this study, we are interested in quantifying the values of the electron mobility and its anisotropy, but also how much it varies with mechanical deformation. Fig. 3 shows a strong growth of  $\mu_y$  with increasing  $\varepsilon_x$  and a slower increase of  $\mu_x$  with increasing  $\varepsilon_y$ . In contrast,  $\mu_x$  decreases with increasing  $\varepsilon_x$  and  $\mu_y$  decreases with increasing  $\varepsilon_y$ . Therefore, the mobility increases under perpendicular strains but is reduced under parallel uniaxial deformations. The enhancements upon compressions of 4% are 51.73% along the *x* axis and 45.00% along the *y* axis, while the correspondent percentual reductions upon 7% stretching are 49.70% and 51.49%. For the biaxial cases, both components of the mobility decrease with increasing strain, which corresponds to the widening the band gap as shown in Fig. 2.

### 3.3 Electronic transport properties

We now discuss the variations of the Seebeck coefficient and the electrical conductivity with strain. Fig. 4 shows the values of the thermopower  $S_y$  in the range of concentrations between  $10^{14}$  and  $10^{20}$  electrons per cm<sup>3</sup>, which is wide enough to cover the range of values reported in the experiments reported in ref. 23, 25 and 26. The variations in both components ( $S_x$  and  $S_y$ ) with respect to all three strains  $\varepsilon_x$ ,  $\varepsilon_y$ , and  $\varepsilon_b$  are shown in Fig. S1 in the ESL.† In all cases, the absolute values of the thermopower decrease with increasing electron concentration following the Mott relation<sup>50</sup> that predicts  $S \propto n^{-2/3}$ . At a concentration of  $2.19 \times 10^{16}$  electron per cm<sup>3</sup>, the principal components of the Seebeck coefficient tensor are  $S_x = -785.56 \mu\text{V K}^{-1}$  and  $S_y = -783.18 \mu\text{V K}^{-1}$  at, which compare fairly well with the  $-850 \mu\text{V K}^{-1}$  at the same concentration measured on nanowhiskers and reported in ref. 23. Moreover, the thermopower seems quite

insensitive to mechanical deformations, with only minor differences (within 2%) for most of the concentrations. Only at very low concentrations of  $10^{14}$  electrons per cm<sup>3</sup> do we find that the thermopower increases significantly.

We now discuss how we choose the relaxation times necessary to obtain numerical values of the electrical conductivity. Our DFT workflow, based on band deformation potentials, predicts electron relaxation times  $\tau_{x,\text{DFT}} = 2825.12$  fs and  $\tau_{y,\text{DFT}} = 302.45$  fs, whereas if we accept the experimental mobility reported in ref. 26,  $\mu_{\text{exp}} = 1132.9 \text{ cm}^2 \text{ V}^{-1} \text{ s}^{-1}$ , and plug it into eqn (2), we obtain the corresponding relaxation times  $\tau_{x,\text{DFT-exp}} = 2826.12$  fs and  $\tau_{y,\text{DFT-exp}} = 302.45$  fs, which in turn yield electrical conductivities at  $0.66 \times 10^{15} \text{ e}^-$  per cm<sup>3</sup> of  $\sigma_{x,\text{DFT-exp}} = 0.46 (\Omega \text{ cm})^{-1}$  and  $\sigma_{y,\text{DFT-exp}} = 0.17 (\Omega \text{ cm})^{-1}$ . Note that the latter is in excellent agreement with the  $0.12 (\Omega \text{ cm})^{-1}$  reported in ref. 26. We therefore opt for this approach, which is justified in view of the inability of the theoretical calculations to capture the complex experimental conditions in terms of substrate, defects, grain boundaries and other kind of lattice imperfection.

Note though that experimental data can also be taken to calculate electron mobilities following the method proposed in ref. 51. This method starts by setting the experimental Seebeck coefficient  $S(T; \mu)$  as an input to determine the reduced chemical potential  $\eta_{\text{eff}}$  from its definition in BoltzTraP

$$S(T; \mu) = \frac{k_B}{q} \frac{2 + \lambda}{1 + \lambda} \frac{F_{1+\lambda}(\eta_{\text{eff}})}{F_{\lambda}(\eta_{\text{eff}})} - \eta_{\text{eff}} \quad (7)$$

where  $\mu$  is the chemical potential,  $\lambda = 1/2$  is the scattering exponent,  $q$  is  $-e$  for electrons and  $+e$  for holes,  $\eta_{\text{eff}} = (\mu - E_b)/k_B T$  with  $E_b$  being the valence band maximum for holes and the conduction band minimum for electrons, and  $F_{1+\lambda}$  are the Fermi functions given by

$$F_j(\eta) = \int_0^{\infty} \frac{e^{\eta} d\varepsilon}{1 + e^{\varepsilon - \eta}} \quad (8)$$

In our case, we use the Seebeck coefficient component  $S_y = -850 \mu\text{V K}^{-1}$  reported in ref. 23; in eqn (7) to find a reduced chemical potential of  $\eta_{\text{eff}} = -9.74$ . We then plug this value in the following expression

$$n(T; \mu) = \frac{1}{2\pi^2} \left( \frac{2m_S^*(T; \mu)k_B T}{\hbar^2} \right)^{3/2} F_{1/2}(\eta_{\text{eff}}) \quad (9)$$

with an electron concentration  $n = 1.01 \times 10^{16} \text{ e}^-$  per cm<sup>3</sup> given by our BoltzTraP calculations at 300 K for the unstrained case and determine an effective mass  $m^* = 1.85m_0$ , where  $m_0$  is the electron rest mass ( $=9.11 \times 10^{-31}$  kg). This value is 8.04 higher than that we find using deformation potential theory ( $0.23m_0$ ). Then, if we insert the BoltzTraP's effective mass in eqn (3), the electron mobility is  $\mu_y = 45.64 \text{ cm}^2 \text{ V}^{-1} \text{ s}^{-1}$  and, in turn, a relaxation time  $\tau_y = 48.02$  fs. The electron mobility is now in the same order of magnitude with the experimental value of  $25.79 \text{ cm}^2 \text{ V}^{-1} \text{ s}^{-1}$ . Therefore, this procedure yields a more accurate estimation of electron mobilities and relaxation times provided that the in-plane Seebeck coefficients are measured. In our case, only the *y*-component is known of the Seebeck



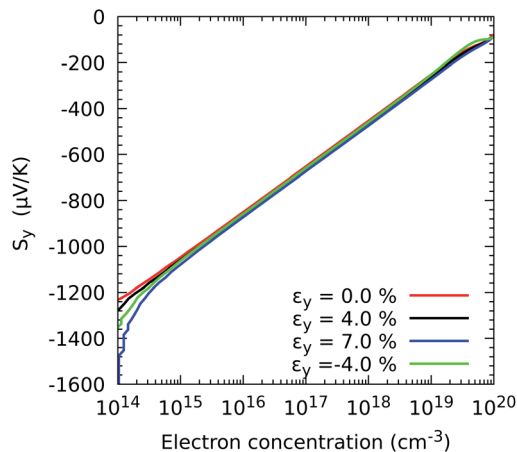


Fig. 4 Effect of the electron concentration on the directional Seebeck coefficient  $S_y$  when strain is applied in the  $y$  direction of  $ZrS_3$  monolayers.

coefficient, which precludes using the method as we need to value along the  $x$ -axis, from which we can determine the relaxation times in both directions.

Having chosen appropriate relaxation times, we now illustrate the characteristic response of the electrical conductivity with respect to electron concentration and strain. The response of the in-plane component  $\sigma_y$  vs.  $\epsilon_y$  is depicted in Fig. 5, and all combinations of in-plane components  $\sigma_x$  and  $\sigma_y$  vs.  $\epsilon_x$ ,  $\epsilon_y$  and  $\epsilon_b$  are shown in Fig. S2.† For uniaxial strains, each component experiences higher changes when the compression is parallel to the mechanical deformation. For instance the component  $\sigma_x$  increases by a factor of 2.87 with an  $\epsilon_x$  of  $-4\%$  and by 3.40 with an  $\epsilon_b$  of  $-4\%$ , and the component  $\sigma_y$  by 2.27 under an  $\epsilon_y$  of  $-4\%$ , at  $0.66 \times 10^{15}$  electron per  $cm^3$ . Therefore, these enhancements evidence not only the possibility of improving the electronic transport by narrowing the band gap but also by increasing electron mobility. Specifically, the most remarkable improvements in electrical conductivity are detected when the electron

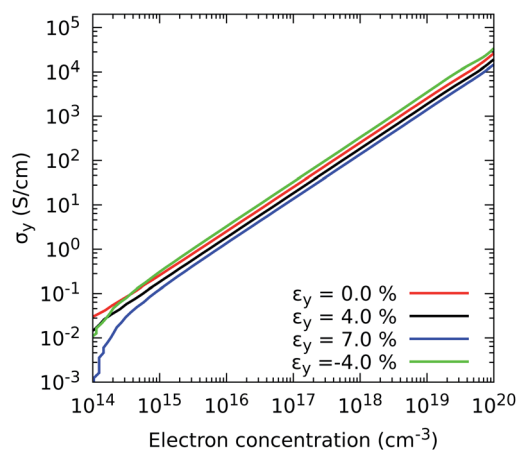


Fig. 5 Effect of electron concentration on the directional electrical conductivity  $\sigma_y$  when strain is applied in the  $y$  direction of  $ZrS_3$  monolayers.

mobility grows by nearly 50% upon 4% compression of the monolayer.

### 3.4 Thermal transport properties

As a transition from electronic to thermal properties, we now examine the response of the electronic contribution  $\kappa_{el}$  to the thermal conductivity calculated with BoltzTraP under deformations. Here we are interested in reducing this contribution to improve the figure of merit. The reduction in  $\kappa_{el}$  occurs under tensile deformations that widen the band gap, and thus diminish the electrical conductivity. The decrease of the electrical conductivity causes a reduction in  $\kappa_{el}$  according to the Wiedemann–Franz law

$$\kappa_{el} = L\sigma T, \quad (10)$$

where  $L$  is the Lorentz number, nominally equal to  $L = \pi^2 k_B^2 / 3e^2 = 2.45 \times 10^{-8} \text{ W } \Omega \text{ K}^{-2}$  but which takes different values for semiconductors.<sup>52</sup>

Fig. 6 and S3† show that strains applied along the  $x$  and  $y$  axes induce a similar response of the components  $\kappa_{el}^{xx}$  and  $\kappa_{el}^{yy}$  to those exhibited by their electrical conductivity counterparts, *i.e.*, shrinking the  $ZrS_3$  nanosheet results in an enhancement of thermal transport by electrons, whereas stretching it reduces the amount of heat carried by these particles. Note that for concentrations higher than  $10^{17}$  electrons per  $cm^3$ , the heat transferred by electrons is comparable to that carried by phonons, as we show next. For instance, for the undeformed case,  $\kappa_{el}^{xx}$  requires a concentration of  $1.20 \times 10^{17}$  electron per  $cm^3$  to reach a value of  $1.15 \text{ W m}^{-1} \text{ K}^{-1}$ , while  $\kappa_{el}^{yy}$  requires a concentration of  $5.75 \times 10^{17}$  electron per  $cm^3$ .

We now analyse the effects of deforming  $ZrS_3$  on phonon transport. We first show in Fig. 7 how the phonon dispersion curves change under biaxial strains of  $-4\%$  and  $7\%$ . In particular, we draw the lowest-lying branches between  $\Gamma = [0.0, 0.0, 0.0]$  and  $Y = [0.125, 0.0, 0.0]$  to illustrate how these curves change near the zone centre when the rotational symmetry is

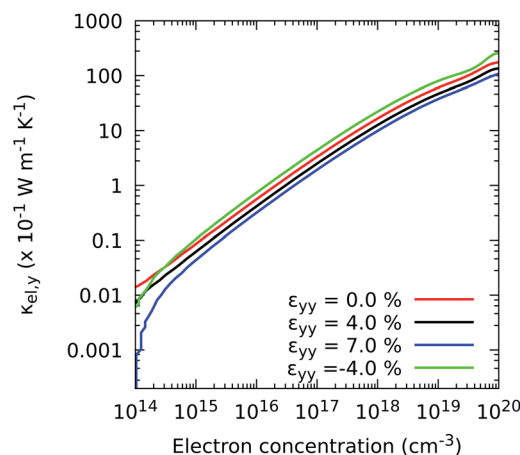


Fig. 6 Effect of the electron concentration on the directional electronic contribution to the thermal conductivity  $\kappa_{el,y}$  when strain is applied in the  $y$  direction.



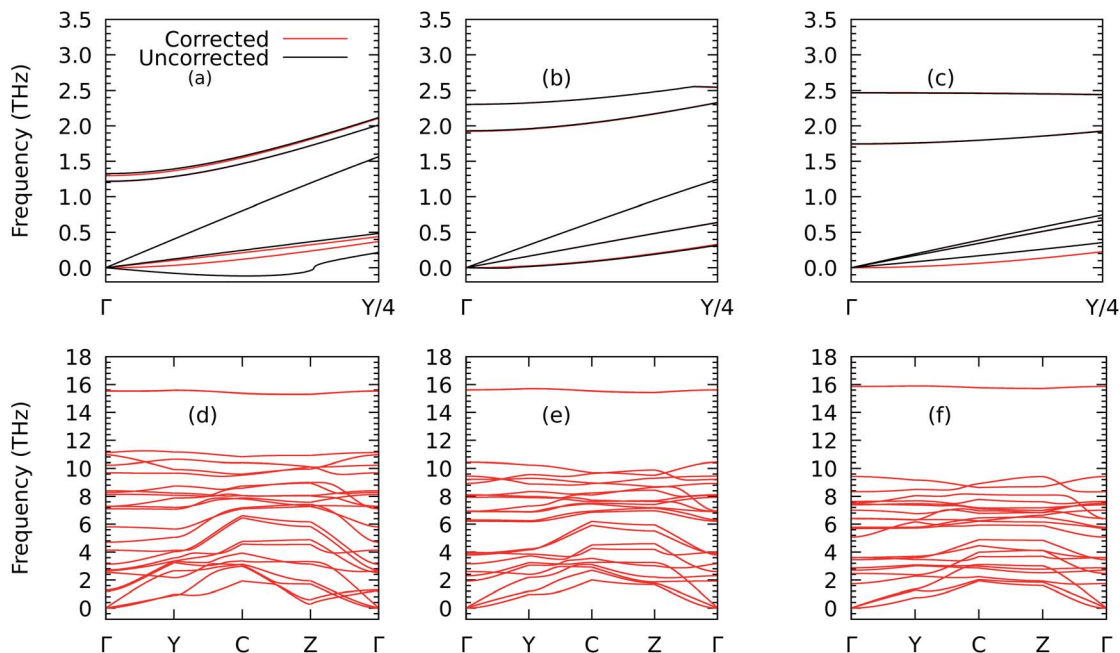


Fig. 7 Details of the phonon dispersions from  $\Gamma = [0, 0, 0]$  to  $Y = [1/2, 0, 0]$  before (in black) and after (in red) correcting the harmonic IFCs according to the procedure given in ref. 40 for the  $ZrS_3$  monolayer for biaxial strains of  $-4\%$  (a),  $0\%$  (b), and  $+7\%$  (c) and their corresponding full views in (d), (e), and (f) along the path  $\Gamma$ -Y-C-Z- $\Gamma$ , where C =  $[1/2, 1/2, 0]$  and Z =  $[0, 1/2, 0]$ .

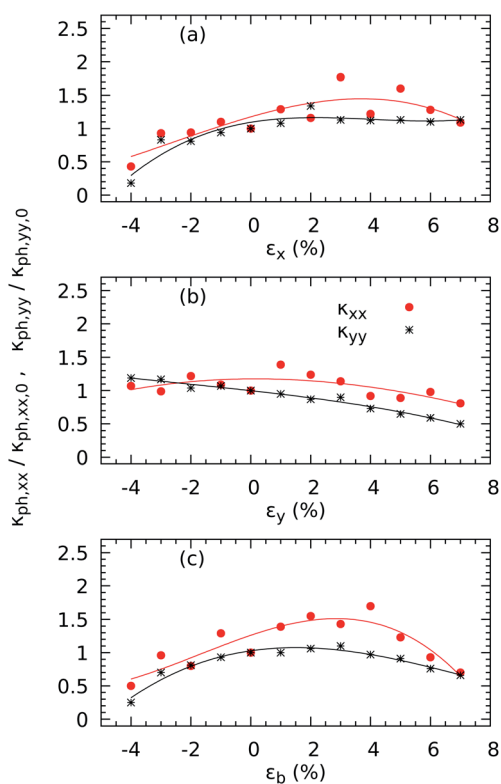


Fig. 8 Effect of strain on the directional phononic contributions to the thermal conductivity  $\kappa_{ph,xx}$  and  $\kappa_{ph,yy}$  at 300 K when strain is applied in the x (a) and y (b) directions (b) and along both axes (c) of  $ZrS_3$  monolayers.  $\kappa_{ph,xx}$  and  $\kappa_{ph,yy}$  are normalized with respect to their corresponding values  $\kappa_{ph,xx,0}$  and  $\kappa_{ph,yy,0}$  for the undeformed case. Solid lines represent smoothing splines, intended to highlight general trends in the data.

restored, as described above. The results underscore the importance of this correction since, going by the raw results of the phononic calculations, a pocket of negative frequencies forms which would point to the presence of mechanical instabilities. Those disappear when the proper correction is applied and would also look unlikely in view of the fact (see Fig. S4†) that we are working in the elastic regime, with perpendicular deformations in x and y created in the monolayer as a response to the correspondent strain exerted in y and x that follow a linear relationship. As a result, we can extract the Poisson's ratios  $\nu_{xy} = 0.12$  and  $\nu_{yx} = 0.18$ . The correction is also important to obtain reasonable values of the lattice thermal conductivity.<sup>18,42</sup>

We then plot the components  $\kappa_{ph,xx}$  and  $\kappa_{ph,yy}$  of the thermal conductivity tensor (as calculated from the corrected force constants) in Fig. 8 to illustrate their different responses to uniaxial and biaxial stresses. When the monolayer is compressed by  $-4\%$  along the x axis, both components decrease, down to 56.75% for  $\kappa_{ph,xx}$  and 82.25% for  $\kappa_{ph,yy}$  with respect to their zero-strain values of  $18.65 \text{ W m}^{-1} \text{ K}^{-1}$  along the x-axis and  $35.12 \text{ W m}^{-1} \text{ K}^{-1}$  along the y-axis. Meanwhile, a tensile  $\epsilon_x$  has no significant effect on either in-plane conductivity. Along the y-axis, both components decrease with increasing strain, down to 7.49% of the original value for  $\kappa_{ph,xx}$  and 19.20% of the no-strain value for  $\kappa_{ph,yy}$  with  $\epsilon_y = -4\%$ . Nonetheless, the most significant effects are seen under biaxial strains  $\epsilon_b$ : a compression of 7% causes both conductivities to decrease by 49.62% for  $\kappa_{ph,xx}$  and 74.93% for  $\kappa_{ph,yy}$ , and a compression  $\epsilon_b = 4\%$  decreases  $\kappa_{ph,xx}$  by 30.05% and  $\kappa_{ph,yy}$  by 34.28%. We note that the thermal transport along the x



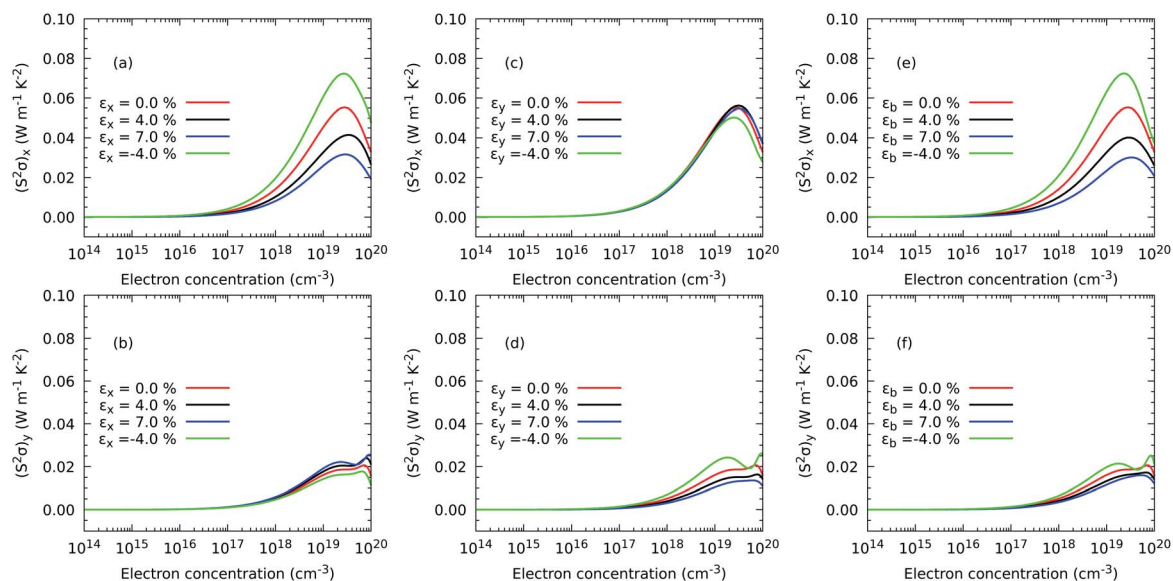


Fig. 9 Effect of electron concentration on the directional power factor  $(S^2\sigma)_x$  (a and c) when strain is applied in the x direction and  $(S^2\sigma)_y$  (b and d) in the y direction and in both axes (e and f) of  $\text{ZrS}_3$  monolayers.

direction is enhanced for intermediate stretching as  $\kappa_{\text{ph},xx}$  increases by a factor of 1.29 with  $\varepsilon_x = 1\%$  and 1.70 for with  $\varepsilon_b = 4\%$ .

Since our study is intended to find those cases in which the figure of merit can be enhanced due to a reduction in the thermal transport, we now perform a deeper analysis of how strain reduces the thermal conductivity at 4% compression and at 7% stretching. According to eqn (6), changes in the thermal conductivity must be correlated to variations in the frequencies, group velocities or lifetimes of phonons. We show in Tables S1–S4† that the group velocities of the six lowest-lying branches (as a sample of the modes that carry most of the heat) vary significantly near  $\Gamma$  for uniaxial and biaxial deformations. However,

not all of these group velocities are reduced upon compression. Therefore, we make a modal decomposition of the thermal conductivities (see Fig. S6 and S7† for details) and find that the lower frequencies contribute less when the monolayer is shrunk by 4%. Additionally, we show in Fig. S6† that heat capacities can be enhanced by a factor of up to 1.07 with  $\varepsilon_b = -4\%$ , decreasing with increasing strain in both uniaxial and biaxial scenarios.

### 3.5 Thermoelectric efficiency: power factor and figure of merit

Finally, once all the thermal and charge transport properties are calculated, we analyse the behavior of the power factor  $S^2\sigma$  and the figure of merit. The former describes the maximum amount

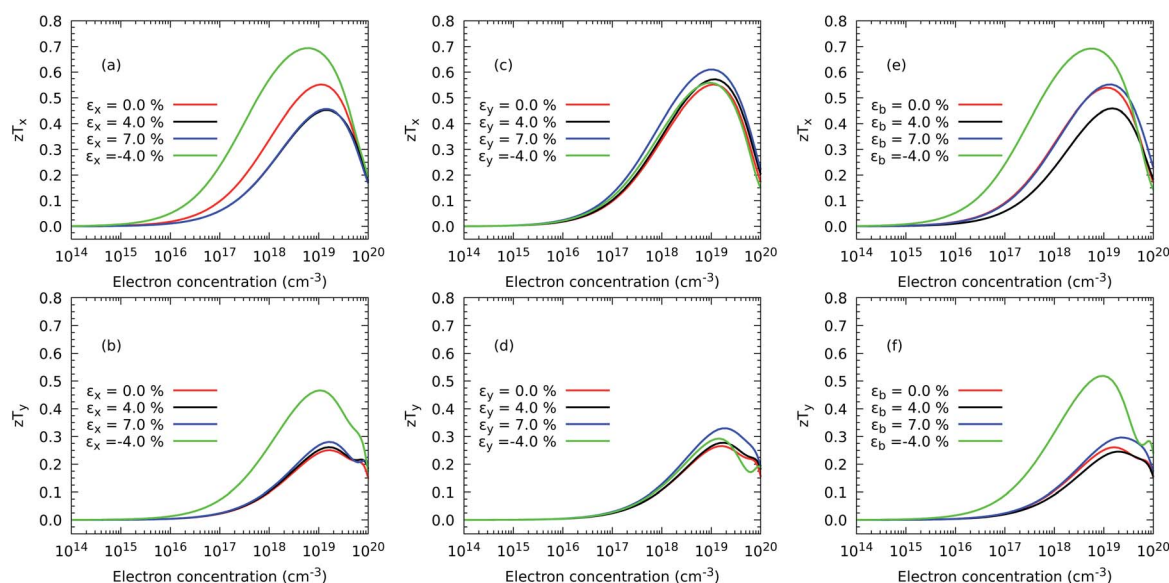


Fig. 10 Effect of electron concentration on the directional figure of merit ( $zT$ ) (a and c) at 300 K when strain is applied in the x direction and ( $zT$ ) (b and d) in the y direction and in both axes (e and f) of  $\text{ZrS}_3$  monolayers.



of electrical power generated by a temperature difference  $\Delta T$ , while the latter gives an idea of the efficiency of this conversion. Fig. 9 illustrates the behaviour of the power factor with strain. We predict that the generation of power is significantly enhanced only for a few values of the strain. In particular,  $(S^2\sigma)_x$  is maximum for  $\varepsilon_x$  and  $\varepsilon_b$  equal to  $-4\%$ , and to a lower extent  $(S^2\sigma)_y$  is maximized by an  $\varepsilon_y$  equal to  $-4\%$ . As we have recently observed for  $\text{TiS}_3$  monolayers,<sup>17</sup> the behaviour of the power factor is driven by changes in the electrical conductivity caused by the widening of the electronic band gap under stretching.

A similar picture is also exhibited by the figure of merit in Fig. 10, with the addition now that the component  $(zT)_y$  is also enhanced under  $\varepsilon_x = \varepsilon_y = -4\%$  as a result of depressed thermal transport caused by a shrinking of the monolayer. Although the absolute values of  $S^2\sigma$  and  $zT$  depend on the choice of the relaxation time, our calculations predict that compression is successful at increasing the maximum value of  $zT$  with respect to the case with no stress applied on the atomic structure. In particular, the maximum  $(zT)_x$  increases from 0.55 with  $1.10 \times 10^{19}$  electron per  $\text{cm}^3$  under no strain to 0.69 with  $6.72 \times 10^{18}$  electron per  $\text{cm}^3$  under a compressive strain  $\varepsilon_x = -4\%$  and to 0.69 with  $5.06 \times 10^{18}$  electron per  $\text{cm}^3$  and  $\varepsilon_b = -4\%$ , representing improvements of nearly 25% in both cases. A more striking result is obtained for the maximum  $(zT)_y$ , which grows from 0.25 with  $1.66 \times 10^{19}$  electron per  $\text{cm}^3$  under no deformation to 0.47 with  $1.05 \times 10^{19}$  electron per  $\text{cm}^3$  applying  $\varepsilon_x = -4\%$  and to 0.52 at  $9.96 \times 10^{19}$  electron per  $\text{cm}^3$ , representing a rise of 86.06% and 107.00%, respectively. Based on these relative results, our DFT methodology is able to suggest a recipe to produce substantial improvements in the thermoelectric efficiency of  $\text{ZrS}_3$  due mostly to the reduction of the phonon thermal transport but also to a higher electrical conductivity.

## 4 Conclusions

In summary, we have calculated the electronic and thermal transport properties of  $\text{ZrS}_3$  monolayers under uniaxial and biaxial strains between  $-4.0\%$  and  $7.0\%$  using first-principles calculations based on density functional theory and the hybrid functional HSE06. Our results indicate that the electronic band gap decreases substantially when compressing in the  $y$ -direction or in both directions simultaneously. For instance, in the former case the band gap can be reduced by 25%, from 1.98 to 1.49 eV, by shrinking the lattice by 4%. They also suggest that the band gap behaves similarly under biaxial stresses to the situation with uniaxial strain along the  $y$ -axis. Furthermore, we analyse the influence of mechanical strain on the electron mobilities by using deformation potential theory, which allows us to determine the electron relaxation times. Our calculations predict small changes in the Seebeck coefficient as metallic behaviour emerges, since the band gap is still present even for the tightest compressions. In contrast, the electrical conductivity exhibits higher variations upon shrinking of the monolayer with, for instance, its component  $\sigma_x$  growing by up to a factor of 3.40 under a biaxial compression of  $-4\%$ , evidencing a relationship between an improvement of the electronic transport and the electron mobility. Furthermore, we have

evaluated the electronic contribution to the thermal conductivity and determined that, even though it can be tuned through strain, its values require a doping level of at least  $10^{19}$  electron per  $\text{cm}^3$  to compete with thermal transport by phonons. Meanwhile, the phononic contribution to the thermal conductivity shows a strong dependence on the direction and intensity of the mechanical applied. This contribution is highly anisotropic, with absolute values of the in-plane components of  $\kappa_{\text{ph},xx} = 18.65 \text{ W m}^{-1} \text{ K}^{-1}$  and  $\kappa_{\text{ph},yy} = 35.12 \text{ W m}^{-1} \text{ K}^{-1}$  at 300 K. We have found that the most successful strategy to reduce these values is to apply biaxial compressions of 4% and tensions of 7%. Finally, our predicted figure of merit at 300 K can be enhanced by 86.06% along the  $x$ -axis and 107.00% in the  $y$ -direction under a unidirectional compression of 4% along  $x$ .

Overall, our calculations suggest that using strain to engineer the band gap and, more generally, the thermoelectric behaviour of a monolayer requires careful consideration of the direction along which deformation is applied. We note that possible buckling under compressive strain is outside the scope of this study, although the lack of imaginary phonon frequencies in our calculations suggests that the shrinkages that we propose should be achievable without inducing buckling.

## Conflicts of interest

There are no conflicts to declare.

## Acknowledgements

We acknowledge the financial support received from the European Union's Horizon 2020 research and innovation programme under grant agreement No. 793726 (TELIOTES – Thermal and electronic transport in inorganic-organic thermoelectric superlattices), from the Ministerio de Economía, Industria y Competitividad (MINECO) under grant FEDER-MAT2017-90024-P and the Severo Ochoa Centres of Excellence Program Grant SEV-2015-0496, and from the Generalitat de Catalunya under grant no. 2017 SGR 1506. We also acknowledge the support from The Supercomputing Center of Galicia (CESGA), where the calculations have been made, and the fruitful discussions with Dr Andrés Castellanos-Gomez.

## References

- 1 N. V. Morozova, I. V. Korobeinikov, K. V. Kurochka, A. N. Titov and S. V. Ovsyannikov, *J. Phys. Chem. C*, 2018, **122**, 14362–14372.
- 2 Y. Wu, Z. Chen, P. Nan, F. Xiong, S. Lin, X. Zhang, Y. Chen, L. Chen, B. Ge and Y. Pei, *Joule*, 2019, **3**, 1276–1288.
- 3 V. M. Pereira and A. C. Neto, *Phys. Rev. Lett.*, 2009, **103**, 046801.
- 4 D. Zhang, K. Zhang, Y. Wang, Y. Wang and Y. Yang, *Nano Energy*, 2019, **56**, 25–32.
- 5 A. Taheri, C. Da Silva and C. H. Amon, *Phys. Chem. Chem. Phys.*, 2018, **20**, 27611–27620.



- 6 A. Castellanos-Gomez, R. Roldán, E. Cappelluti, M. Buscema, F. Guinea, H. S. van der Zant and G. A. Steele, *Nano Lett.*, 2013, **13**, 5361–5366.
- 7 G. Li, K. Yao and G. Gao, *Nanotechnology*, 2017, **29**, 015204.
- 8 R. D'Souza, S. Mukherjee and S. Ahmad, *J. Appl. Phys.*, 2019, **126**, 214302.
- 9 L. Brattas and A. Kjekshus, *Acta Chem. Scand.*, 1972, **26**, 3441–3449.
- 10 S. Furuseth, L. Brattas and A. Kjekshus, *Acta Chem. Scand.*, 1975, **29**, 623.
- 11 J. O. Island, A. J. Molina-Mendoza, M. Barawi, R. Biele, E. Flores, J. M. Clamagirand, J. R. Ares, C. Sánchez, H. S. van der Zant, R. D'Agosta, *et al.*, *2D Mater.*, 2017, **4**, 022003.
- 12 Y. Jin, X. Li and J. Yang, *Phys. Chem. Chem. Phys.*, 2015, **17**, 18665–18669.
- 13 Y. Saeed, A. Kachmar and M. A. Carignano, *J. Phys. Chem. C*, 2017, **121**, 1399–1403.
- 14 R. Biele, E. Flores, J. R. Ares, C. Sanchez, I. J. Ferrer, G. Rubio-Bollinger, A. Castellanos-Gomez and R. D'Agosta, *Nano Res.*, 2018, **11**, 225–232.
- 15 R. Roldán, A. Castellanos-Gomez, E. Cappelluti and F. Guinea, *J. Phys.: Condens. Matter*, 2015, **27**, 313201.
- 16 X. Meng, T. Pandey, J. Jeong, S. Fu, J. Yang, K. Chen, A. Singh, F. He, X. Xu, J. Zhou, W.-P. Hsieh, A. K. Singh, J.-F. Lin and Y. Wang, *Phys. Rev. Lett.*, 2019, **122**, 155901.
- 17 F. Saiz and R. Rurali, *Nano Express*, 2020, **1**, 010026.
- 18 F. Saiz, J. Carrete and R. Rurali, *Nanomaterials*, 2020, **10**, 704.
- 19 C. Wang, C. Zheng and G. Gao, *J. Phys. Chem. C*, 2020, **124**, 6536–6543.
- 20 J. O. Island, R. Biele, M. Barawi, J. M. Clamagirand, J. R. Ares, C. Sánchez, H. S. Van Der Zant, I. J. Ferrer, R. D'Agosta and A. Castellanos-Gomez, *Sci. Rep.*, 2016, **6**, 1–7.
- 21 J. Zhang, X. Liu, Y. Wen, L. Shi, R. Chen, H. Liu and B. Shan, *ACS Appl. Mater. Interfaces*, 2017, **9**, 2509–2515.
- 22 J. Heyd, G. E. Scuseria and M. Ernzerhof, *J. Chem. Phys.*, 2003, **118**, 8207–8215.
- 23 G. Perluzzo, A. Lakhani and S. Jandl, *Solid State Commun.*, 1980, **35**, 301–304.
- 24 E. Flores, J. R. Ares, I. J. Ferrer and C. Sánchez, *Phys. Status Solidi RRL*, 2016, **10**, 802–806.
- 25 R. Späh, M. Lux-Steiner, E. Bucher and S. Wagner, *Appl. Phys. Lett.*, 1984, **45**, 744–745.
- 26 K. R. Patel, *Int. J. Phys., Chem. Math. Sci.*, 2012, **2**, 74–85.
- 27 G. Kresse and J. Hafner, *Phys. Rev. B: Condens. Matter Mater. Phys.*, 1993, **47**, 558–561.
- 28 G. Kresse and J. Hafner, *Phys. Rev. B: Condens. Matter Mater. Phys.*, 1994, **49**, 14251–14269.
- 29 G. Kresse and J. Furthmüller, *Comput. Mater. Sci.*, 1996, **6**, 15–50.
- 30 G. Kresse and J. Furthmüller, *Phys. Rev. B: Condens. Matter Mater. Phys.*, 1996, **54**, 11169–11186.
- 31 J. P. Perdew, K. Burke and M. Ernzerhof, *Phys. Rev. Lett.*, 1996, **77**, 3865–3868.
- 32 P. E. Blöchl, *Phys. Rev. B: Condens. Matter Mater. Phys.*, 1994, **50**, 17953–17979.
- 33 G. Kresse and D. Joubert, *Phys. Rev. B: Condens. Matter Mater. Phys.*, 1999, **59**, 1758–1775.
- 34 S. Grimme, J. Antony, S. Ehrlich and H. Krieg, *J. Chem. Phys.*, 2010, **132**, 154104.
- 35 G. K. Madsen and D. J. Singh, *Comput. Phys. Commun.*, 2006, **175**, 67–71.
- 36 J. Bardeen and W. Shockley, *Phys. Rev.*, 1950, **80**, 72.
- 37 J. Carrete, B. Vermeersch, A. Katre, A. van Roekeghem, T. Wang, G. K. Madsen and N. Mingo, *Comput. Phys. Commun.*, 2017, **220**, 351–362.
- 38 A. Togo and I. Tanaka, *Scr. Mater.*, 2015, **108**, 1–5.
- 39 W. Li, J. Carrete, N. A. Katcho and N. Mingo, *Comput. Phys. Commun.*, 2014, **185**, 1747–1758.
- 40 J. Carrete, W. Li, L. Lindsay, D. A. Broido, L. J. Gallego and N. Mingo, *Mater. Res. Lett.*, 2016, **4**, 204–211.
- 41 P. Torres, F. X. Alvarez, X. Cartoixa and R. Rurali, *2D Mater.*, 2019, **6**, 035002.
- 42 J. Carrete, W. Li, L. Lindsay, D. A. Broido, L. J. Gallego and N. Mingo, *Mater. Res. Lett.*, 2016, **4**, 204–211.
- 43 T. Sohler, M. Gibertini, M. Calandra, F. Mauri and N. Marzari, *Nano Lett.*, 2017, **17**, 3758–3763.
- 44 M. D. Luca, X. Cartoixa, D. Indolese, J. Martín-Sánchez, K. Watanabe, T. Taniguchi, C. Schoenenberger, R. Trotta, R. Rurali and I. Zardo, *2D Mater.*, 2020, **7**, 035017.
- 45 J. Carrete, B. Vermeersch, A. Katre, A. van Roekeghem, T. Wang, G. K. Madsen and N. Mingo, *Comput. Phys. Commun.*, 2017, **220**, 351–362.
- 46 W. Li, L. Lindsay, D. A. Broido, D. A. Stewart and N. Mingo, *Phys. Rev. B: Condens. Matter Mater. Phys.*, 2012, **86**, 174307.
- 47 P. Torres, A. Torelló, J. Bafaluy, J. Camacho, X. Cartoixa and F. X. Alvarez, *Phys. Rev. B*, 2017, **95**, 165407.
- 48 S. Tamura, *Phys. Rev. B: Condens. Matter Mater. Phys.*, 1983, **27**, 858–866.
- 49 H. Yi, S. J. Gilbert, A. Lipatov, A. Sinitskii, J. Avila, J. Abourahma, T. Komesu, M. C. Asensio and P. A. Dowben, *J. Phys.: Condens. Matter*, 2020, **32**, 29LT01.
- 50 H. Lee, *Thermoelectric: Design and Materials*, 2017.
- 51 Z. M. Gibbs, F. Ricci, G. Li, H. Zhu, K. Persson, G. Ceder, G. Hautier, A. Jain and G. J. Snyder, *npj Comput. Mater.*, 2017, **3**, 1–7.
- 52 G. Chester and A. Thellung, *Proc. Phys. Soc., London*, 1961, **77**, 1005.

